Contents lists available at ScienceDirect

Journal of Non-Newtonian Fluid Mechanics

journal homepage: www.elsevier.com/locate/jnnfm





Suppression of vortex-induced vibrations of a cylinder in inertial-elastic flow

Pieter R. Boersma, Jonathan P. Rothstein, Yahya Modarres-Sadeghi *

Department of Mechanical and Industrial Engineering, University of Massachusetts Amherst, Amherst, 01002, MA, USA

ARTICLE INFO

Keywords: Vortex-induced vibration Viscoelastic flow Suppression

ABSTRACT

We study Vortex-Induced Vibration (VIV) of a one-degree-of-freedom cylinder placed in inertial-elastic flows experimentally. We show that there is a critical Reynolds number for the onset of VIV in these flows and this critical Reynolds number increases when the elasticity in the fluid is increased. We also show that at a constant Reynolds number, adding elasticity to the fluid reduces the amplitude of oscillations and eventually suppresses VIV entirely. For the cases where VIV is observed, the onset of the lock-in range does not depend on the Reynolds number, as a result of the competing effects of shear-thinning and elasticity. The vortices that are observed in the wake are significantly different from those observed in Newtonian VIV: the vortices are S-shaped with relatively long tails that influence the formation of the vortices that are formed in the following cycle.

1. Introduction

A flexibly-mounted rigid cylinder placed in flow constitutes a model problem in Fluid-Structure Interactions (FSI). Above a critical Reynolds number, defined as $Re = \rho U D/\mu$, where ρ is the fluid density, U is the free-stream velocity, D is the cylinder diameter, and μ is the dynamic viscosity of the fluid, vortices are shed in the wake of the cylinder. If the shedding frequency equals the system's natural frequency, the cylinder oscillates. The synchronization between the natural frequency and the shedding frequency occurs over a range of reduced velocities, defined as $U^* = U/f_n D$ where f_n is the structure's natural frequency, and the U^* range where this synchronization is observed is called the lock-in range. The observed oscillations in the lock-in range are called vortex-induced vibrations (VIV) [1-3]. If the cylinder is allowed to oscillate only in the direction perpendicular to the flow, or the crossflow direction, large oscillations, on the order of one cylinder diameter, can be observed [4,5]. A subcritical response has also been observed in the crossflow VIV, where synchronization between the vortex shedding frequency and the cylinder oscillation frequency occur at Reynolds numbers below the critical Reynolds number for shedding in the wake of a fixed cylinder ($Re_{cr,fixed} = 47$ [6]). The critical Reynolds number for a flexibly-mounted cylinder in crossflow has been shown both numerically and experimentally to be $Re_{cr} = 19$ [7–9]. Up until very recently, VIV had only been studied in Newtonian fluids. In this paper, we will investigate the non-Newtonian effects of fluid viscoelasticity on the VIV response of a flexibly-mounted cylinder.

The influence of viscoelasticity on the vortex shedding from a fixed cylinder has been studied both numerically and experimentally.

Coelho and Pinho [10] studied the effect of shear-thinning, weakly elastic fluids on the generation of vortices in the wake of a fixed cylinder in the Reynolds number range of 50 < Re < 9000. They found that shear-thinning reduces the boundary layer thickness and vortex formation length. This leads to an increase in the vortex shedding frequency and by extension, the Strouhal number, defined as $St = f_s D/U$, where f_s is the vortex shedding frequency. Fluid elasticity has the opposite effect, where the formation length is increased and the shedding frequency and Strouhal number are reduced [11-14]. Lashgari et al. [15] studied numerically the wake instability of a fixed cylinder in power-law thinning flow. They found that shear-thinning reduces the stability of the boundary layer and the vorticity close to the cylinder is intensified. Hamid et al. [16] discussed the influence of a viscoelastic fluid on the flow structures behind a fixed cylinder in the inertial-elastic regime. Through dynamic mode decomposition (DMD), they observed the stretching of the shear layers and the suppression of the vortex shedding frequency. The energy associated with each DMD mode decreases with fluid viscoelasticity, which suppresses velocity fluctuations when compared with Newtonian fluids.

As shown for the case of the fixed cylinder, often the effects of shear-thinning and elasticity can have very different and sometimes competing influences on the flow. To deconvolute the effects of each on the VIV response of a cylinder, we previously conducted experimental [17] and numerical [18] studies that explored the effect of shear-thinning and shear-thickening on the VIV response in the absence of fluid elasticity. In our previous experimental work we investigated the VIV response of a flexibly-mounted cylinder in the cross-flow of

E-mail address: modarres@engin.umass.edu (Y. Modarres-Sadeghi).

Corresponding author.

inelastic shear-thinning Xanthan gum solutions [17]. In that work, we studied a wide range of concentrations of Xanthan gum in water. The rheology of these fluids were found to be well described by a powerlaw fluid both in shear and in extension. With increasing Xanthan gum concentration and increasing strength of shear-thinning of the fluid viscosity, the VIV response was found to be increasingly suppressed with the onset of oscillations being shifted to larger Reynolds numbers, the maximum amplitude of oscillations being reduced, and the lockin range being shifted to lower U^* values. Indeed, at the largest Xanthan gum concentrations tested, no VIV was observed within the accessible range of Reynolds numbers. We showed numerically [18] that by defining a characteristic Reynolds number based on a viscosity evaluated at a characteristic shear rate, $\dot{\gamma} = U/D$, the amplitude of the VIV response, in the reduced velocity ranges where oscillations are observed, stays very similar for the shear-thinning, shear-thickening and Newtonian fluids.

Although viscoelastic effects on VIV have yet to be studied at high Reynolds numbers, Viscoelastic Fluid-Structure Interactions (VFSI) has been studied at vanishingly small Reynolds numbers ($Re \ll 1$) and high Weissenberg numbers. Here, the Weissenberg number is defined as $Wi = \lambda \dot{\gamma}$, where λ is the fluid relaxation time and $\dot{\gamma}$ is the shear rate. The Weissenberg number describes the relative importance of fluid elasticity to fluid viscosity in a flow. Dev et al. [19-23] placed flexible and flexibly-mounted sheets and cylinders in viscoelastic flows where Wi > 1 and $Re \ll 1$. In these viscoelastic flows, the VFSI response is not dominated by inertial shedding of vortices, but by the onset of elastic instabilities that drive oscillations at frequencies equal to the fluid instability frequency. In addition to the experimental work from our group, Hopkins et al. [24] studied multiple thin flexible glass cylinders resembling cilia in a microfluidic flow cell with Wi > 1 and $Re \ll 1$ and found that individual cylinders oscillating through a viscoelastic fluid instability can synchronize and move in unison.

Few studies exist where both elasticity and fluid inertia are relevant to an FSI system, as opposed to the cases where either dominates. Fluid inertia and elasticity are competitive in nature. Inertia causes instabilities downstream of an obstacle [4] while elasticity causes instabilities upstream of an obstacle [25-27], although the instability can depend on the blockage ratio [28]. At a constant Weissenberg number, the size of the separated vortex upstream of an obstacle decreases as the Reynolds number is increased until it disappears completely when the Reynolds and Weissenberg number become comparable [29–31]. As the Reynolds number continues to increase, and the influence of fluid inertia increases, the flow instability can occur downstream of the obstacle, although the strength and nature of the wake is still strongly a function of the fluid properties [32-36]. In addition to fluid inertia and elasticity, fluid rheology is known to have an effect of generation of vortices in the wake of an obstacle [10,37]. Patel et al. [38] studied the forced oscillations of a cylinder in FENE-P and Oldroyd-B fluids at $0.01 \le Wi \le 10$ and Re = 100. In addition to the primary vortices, they observed stretched vorticity bands as Wi is increased. They confirmed that their observation is a new mode of shedding by determining that the bands are rotationally dominated, and that these secondary vortices are formed purely due to the fluid elasticity. They predicted that in a free-to-oscillate VFSI system where fluid inertia and elasticity are important, the oscillation amplitude would be reduced until completely suppressed as the effect of elasticity is increased. Xiong et al. [39] conducted numerical VFSI simulations of a flexibly-mounted rigid cylinder in FENE-P fluid at Reynolds numbers of 30 to 500 and Weissenberg numbers of 0 to 80. They found that as the Weissenberg number or polymer extensibility increases, the VIV response is suppressed and that the oscillation amplitude is more dependent on the Reynolds number, especially at higher Weissenberg numbers, than when in Newtonian flow.

As discussed above, the majority of VIV research has been focused on cases where $Re\gg 1$ and $Wi\ll 1$. Only recently, has a new branch of fluid structure interactions is being explored, where $Re\ll 1$ and

Table 1Consistency indices, power-law exponents, infinite extensional viscosity, and relaxation times for 0.02 and 0.03 g/L Flopaam 3330.

c (g/L)	m (Pa s^n)	n (-)	$\eta_{E,\infty}$ (Pa s)	λ (ms)
0.02	0.010	0.6	2.8	9.4
0.03	0.014	0.6	10.0	14.7

Wi>1. The present work focuses on a region in between, were fluid elasticity and inertia are important, $Re\gg 1$ and Wi>1. A flexibly-mounted cylinder is suspended in a viscoelastic flow. A characteristic Reynolds number and a Weissenberg number are defined and the regions of $Re\gg 1$ and Wi>1 are explored. Comparisons are made to the cases of Newtonian flow and fixed cylinders. The wake is observed through particle image velocimetry (PIV) and the VIV response is recorded through the amplitude and frequency measurements.

2. Fluid rheology

The fluid used in these experiments is Flopaam 3330s (SNF), a high molecular weight, water-soluble polyacrylamide that displays viscosity-thinning and elastic behaviors [40]. The Flopaam is mixed in distilled water (DI) at two concentrations, 0.02 g/L and 0.03 g/L. The shear rheology is measured using a cone-and-plate TA Instruments Discovery HR-3 hybrid rheometer and is shown in Fig. 1(a). Flopaam 3330s is shear-thinning and follows the power law relation, $\eta = m\dot{\gamma}^{n-1}$ [41], where η is the shear viscosity, m is the shear consistency index, $\dot{\gamma}$ in the shear rate, and n is the shear power-law exponent given in Table 1.

Because the viscosity is a function of the fluid deformation, a Reynolds number is defined using a relevant shear viscosity, η , and a relevant characteristic shear rate. A typical shear rate used to describe flow around a cylinder in non-Newtonian fluid at low Reynolds numbers is $\dot{\gamma} = U/D$ [17,18,38,39]. However, at high Reynolds numbers, the shear rate within the boundary layer is typically much larger as the lengthscale of interest is the boundary layer thickness and not the diameter of the cylinder. As a result, in this case, the choice of the appropriate shear rate to describe the flow is not clear a priori. In the results discussed here, Particle Image Velocimetry (PIV) will be used to measure the shear rate close to the cylinder wall and determine the appropriate characteristic shear rate for calculating the Reynolds and Weissenberg numbers. We will show later, in Section 4, that for c = 0.02g/L Flopaam solution, the characteristic shear rate is approximately $\dot{\gamma}_{char} = 4U/D$, while for the c = 0.03 g/L Flopaam solution, the characteristic shear rate is even larger at $\dot{\gamma}_{char} = 8U/D$. The viscosity at the characteristic shear rate is calculated from the power law model fit to the data, $\eta_{char} = m\dot{\gamma}_{char}^{n-1}$. This allows us to define the Reynolds number of the flow as $Re = \rho U D/\eta_{char}$, and to quantify the importance of elasticity by defining a Weissenberg number, $Wi = \lambda \dot{\gamma}_{char}$. For any given fluid, the Weissenberg number and the Reynolds number are coupled and cannot be varied independently. In order to modify the relative importance of inertia to elasticity, the fluid must be changed. One can capture the relative importance of elasticity to inertia with the elasticity number, $El = Wi/Re = \lambda \eta_{char}/\rho D^2$, which has no explicit dependence on flow strength. However, it should be noted that the elasticity number is not a constant since the fluid viscosity is shear thinning and depends on the shear rate. The elasticity number will therefore decrease slightly with increasing Reynolds number and Weissenberg number.

The extensional rheology is measured using dripping onto substrate capillary breakup extensional rheology (CaBER-DoS) [17,42,43]. In CaBER-DoS, a droplet of fluid is ejected from a nozzle at a very slow flow rate. While still attached to the nozzle, the droplet wets a surface just below the tip of the nozzle. As the fluid wets the substrate, the droplet is drawn down from the nozzle, creating a fluid filament that breaks up due to capillary forces. For a viscoelastic fluid, the fluid filament undergoes an elasto-capillary decay, resulting in a diameter

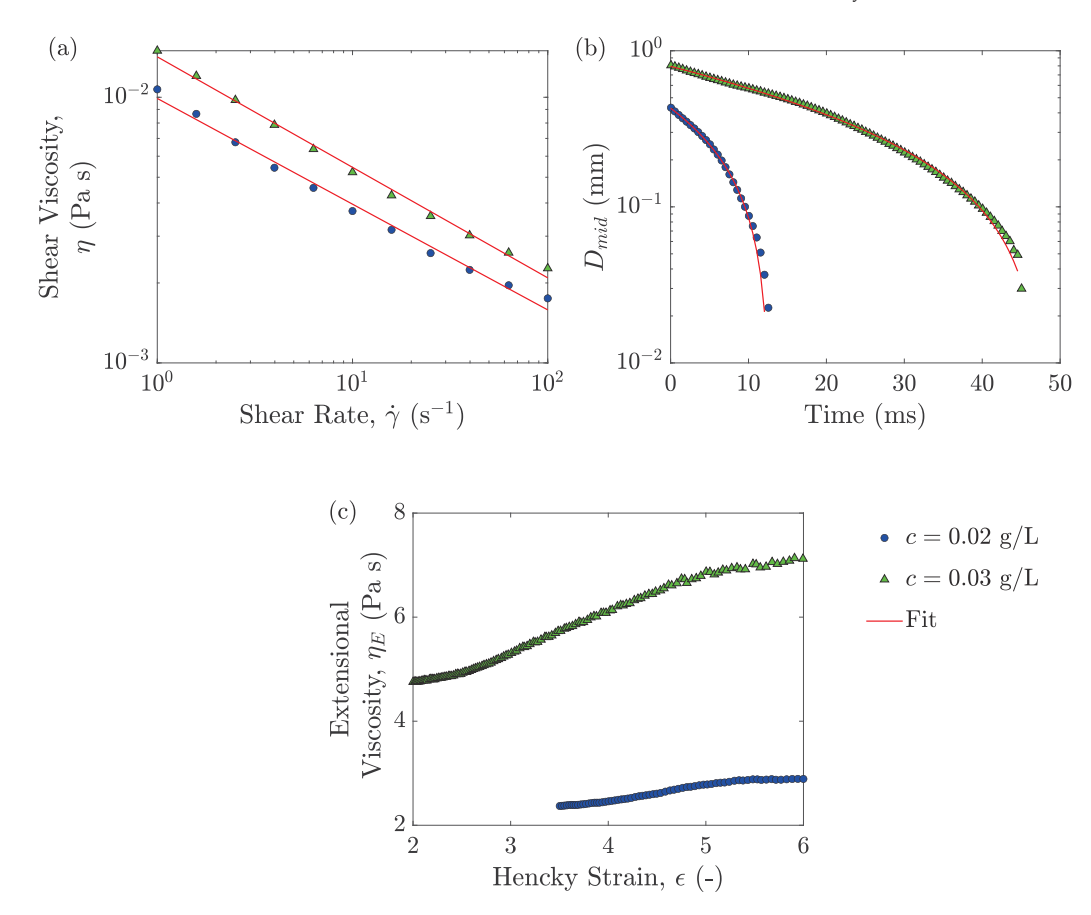


Fig. 1. Rheology of 0.02 g/L (blue circles) and 0.03 g/L (green triangles) Flopaam 3330s at room temperature: (a) Shear viscosity as a function of shear rate with power-law fit, (b) filament diameter thinning during capillary breakup extensional rheology (CaBER) with viscoelastic fit, and (c) calculations of the extensional viscosity as a function of strain showing strain hardening of each fluid.

that decays exponentially with time. The diameter decay is observed by a high-speed camera and then digitized using EdgeHog (KU Leuven), a Matlab program that extracts diameter as a function of time from CaBER-DoS. The diameter decay is shown in Fig. 1(b). The extensional viscosity and relaxation time are determined by first fitting the diameter to $D_{mid}(t) = Ae^{-Bt} - Ct + E$ [44], where A, B, C, and E are fitting parameters and $D_{mid}(t)$ is the fluid filament diameter as a function of time. For an Oldroyd-B fluid, the relaxation time can be extracted from the fitting constants such that $\lambda = 1/(3B)$ [44]. The relaxation times for the two fluids are given in Table 1. The extensional viscosity is calculated by differentiating the fit to the diameter decay such that $\eta_E(t) = -\sigma (dD_{mid}(t)/dt)^{-1}$ [44], where $\sigma = 72$ mN/m is the surface tension of water. The extensional viscosity is plotted in Fig. 1(c) as a function of Hencky strain which is defined as $\epsilon(t)$ = $2ln(D_0/D_{mid}(t))$, where $D_0 = 1.6$ mm is the diameter of the nozzle used in CaBER-DoS [42]. The results show that the extensional viscosity of both fluids are strongly strain hardening with measured extensional viscosity values much larger than the shear viscosity at similar shear rates, $\dot{\gamma} \approx 100 \text{ s}^{-1}$, shown in Fig. 1(a). The resulting Trouton ratios are very large, $Tr = \eta_E/\eta > 1000$, and are consistent with other high molecular weight dilute polymer solutions. Additionally, the final breakup of the fluid filament provides information about the finite extensibility of the polymer. The extensional viscosity in the limit of infinite strain can be calculated from the fit to the diameter decay at long times. It is presented alongside the relaxation time in Table 1.

3. Experimental setup

The experiments were conducted in a rotating water channel comprised of two concentric acrylic cylinders, an acrylic bottom, and an open top, that was spun on its axis by a high torque, low rpm motor (Fig. 2). This design created a flow velocity without the need for pumps and flow straighteners with flow velocities at the center of the channel in the range of 1.8 cm/s to 9.1 cm/s with a resolution of 0.1 cm/s, and 9.1 cm/s to 24 cm/s with a resolution of 0.2 cm/s, depending on the motor that was used. The channel had an outer radius, R_1 , of 30 cm and an inner radius, R_2 , of 23.5 cm, and as a result, a channel width of 4.6 cm with a distance from the center of the cylinder to the center of the channel, R_1 , of 27.7 cm. The set-up was used for tests both on a flexibly-mounted cylinder (Fig. 2(a)), and a fixed cylinder (Fig. 2(b)). More details on this setup can be found in our previous work [8,17].

A rigid aluminum cylinder with D = 0.4 cm was used for the non-Newtonian experiments and a rigid aluminum cylinder with D = 0.2 cm was used in the Newtonian experiments. The cylinder was suspended by two pieces of rectangular spring steel which acted as springs. The reduced velocity, U^* , was varied by varying the natural frequency of the system by adjusting the length of the springs through an adjustable collar. This allowed the Reynolds number to be fixed by holding the flow velocity constant, while changing the reduced velocity. The natural frequency was measured in air using a decay test. The cylinder used in the non-Newtonian experiments had a submerged aspect ratio of 25.75D, was placed 0.75D from the bottom of the channel, and had a blockage ratio of 11.5. The cylinder used in the Newtonian experiments had an aspect ratio of 56.5D, was placed 1.5D from the bottom of the channel, and had a blockage ratio of 23. The springs limited the cylinder's motion to the crossflow direction. The structural damping provided by the springs was measured using a decay test in air and was on the order of 10^{-2} for all spring lengths. The mass-damping coefficient, defined as $m^*\zeta$ where ζ is the damping ratio and m^* is the mass ratio, was on the order of 10⁻¹, which is in the range where

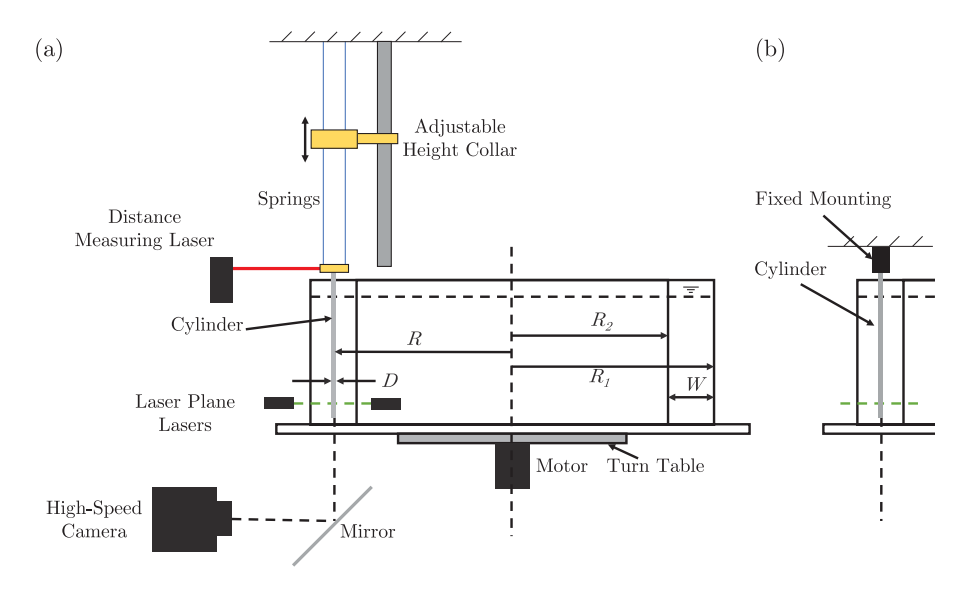


Fig. 2. Schematic of the experimental setup used here, (a) where a flexibly-mounted cylinder is placed in a rotating water channel and can oscillate in a direction perpendicular to the direction of flow, and (b) where the cylinder is fixed at the top and does not oscillate.

relatively large-amplitude oscillations are expected in a Newtonian fluid [4]. The specific values of natural frequencies, damping ratios, and mass ratios for each data point are given in the Appendix (Table A.1 for the Newtonian cases, and Tables A.2 and A.3 for the non-Newtonian cases). In short, these parameters are within the following ranges: $2.3 \le f_n \le 21.8$ Hz, $0.011 \le \zeta \le 0.029$, and $23.1 \le m^* \le 33.3$ for the Newtonian case, and $2.9 \le f_n \le 21.8$ Hz, $0.011 \le \zeta \le 0.029$, and $6.7 \le m^* \le 8.7$ for the viscoelastic cases.

The cylinder's oscillation amplitude and frequency were measured using a high resolution distance measuring laser (Panasonic HL-G11). The flow was visualized by seeding the fluid with 10 μ m neutrally buoyant glass spheres (Dantec Dynamics) and illuminating a horizontal plane with a laser sheet. The flow was captured using a Phantom V4.2 high speed camera and Particle Image Velocimetry (PIV) post-processing was conducted using PIVlab v2.62 [45]. PIVlab was used to calculate the local vorticity, ω , and the shear rate, $\dot{\gamma}$. The expressions for these values are $\omega = \nabla \times u$, where the velocity vector is $u = u_x \hat{i} + u_y \hat{j}$ and $\dot{\gamma} = \partial u_x/\partial y + \partial u_y/\partial x$.

4. The wake of a fixed cylinder

In this section we consider the wake of a fixed cylinder in the two viscoelastic Flopaam solutions for a mean flow velocity range of $1.8 \leq U \leq 24$ cm/s. An example of the wake during the shedding cycle is shown in Fig. 3 for the viscoelastic c=0.02 g/L Flopaam solution at a fixed flow velocity of U=20.3 cm/s. In these plots, the normalized vorticity and strain rate are plotted, where they are normalized by the maximum vorticity in the wake, $\omega_{max}=240$ s⁻¹, and the maximum shear rate in the wake, $\dot{\gamma}_{max}=227$ s⁻¹, respectively, both found by averaging the top 10% maximum of their values over at least 100 frames of the particle image velocimetry (PIV) results. Shear rate is overlayed on the vorticity plot to show where shear rate is high in relation to the vorticity.

The maximum local shear rate that is observed here in the wake of a cylinder is significantly larger than the characteristic shear rate used by Patel et al. [18], $\dot{\gamma}_{max} > U/D$. The relation between maximum shear rate measured through PIV, $\dot{\gamma}_{max}$, and Patel's characteristic shear rate U/D is given in Fig. 4(a) for both viscoelastic fluids over the entire range of flow velocities tested. For the c=0.02 g/L Flopaam solution, a fit to the data shows that the maximum shear rate is linearly proportional to U/D and grows as approximately $\dot{\gamma}_{max}=4U/D$. For the c=0.03 g/L Flopaam solution, a similar trend is observed, but

with a larger slope of $\dot{\gamma}_{max}=8U/D$. This difference means that using a characteristic shear rate of U/D would under-predict the Reynolds number, the Weissenberg number, and the elasticity number of the flow for both fluids. Moving forward, the characteristic shear rate will be defined as the maximum shear rate from the PIV measurements. For c=0.02 g/L Flopaam solution, the characteristic shear rate is thus defined as $\dot{\gamma}_{char}=4U/D$, while for the c=0.03 g/L Flopaam solution, the characteristic shear rate is defined as $\dot{\gamma}_{char}=8U/D$.

The Weissenberg numbers, Wi, and elasticity numbers, El, are shown as a function of Re in Fig. 4. The symbols in the plots refer to the cases with stable separated vortices (square) and vortex shedding (diamond). For comparison, a data point for an inelastic (Wi=0) shear thinning case is also shown in the plot reproduced from Boersma et al. [17]. From these plots, it is observed that Wi and Re are coupled and cannot be varied independently without changing the fluid. Additionally, the Elasticity number, El, decreases slowly with increasing Reynolds number due to the decrease in the shear viscosity with increasing flow velocity and shear rate. Note that the Elasticity number of the more concentrated solution is 2–3 times larger then the less concentrated solution and as such more significant effects of elasticity will be present at lower Reynolds numbers for the c=0.03 g/L Flopaam solution.

Returning to the vortex shedding patterns shown for the c = 0.02g/L Flopaam solution in Fig. 3, we can now define the flow in terms of the appropriate characteristic Reynolds number, Weissenberg number, and Elasticity number, Re = 726, Wi = 2.2, and El = 3.0, respectively. This particular case was chosen because it is the largest Reynolds and Weissenberg number case that could be tested in our flow cell for the c = 0.02 g/L Flopaam solution. As a result, the vortex structure and dynamics are most strongly affected by the elasticity of the fluid and in many ways quite different from the vortex structure observed for a Newtonian fluid [1,3]. For instance, in Fig. 3(a,b), the head of a positive (red) vortex is located quite far from the cylinder at $x/D \sim 4.3$ and $y/D \sim -0.75$. This is different from what has been observed for Newtonian and shear-thinning and shear-thickening fluids for which the vortex formation length is considerably shorter and the vortices shed from much closer to the cylinder [17]. Similar elongated vortices and large vortex formation lengths have been observed previously both numerically and experimentally for flows of viscoelastic liquids [10,16, 38,46]. Another difference observed from Newtonian fluid at a similar Reynolds number is that the vortex heads of positive vorticity do not interact directly with the vortex heads of the opposite sign. As seen in

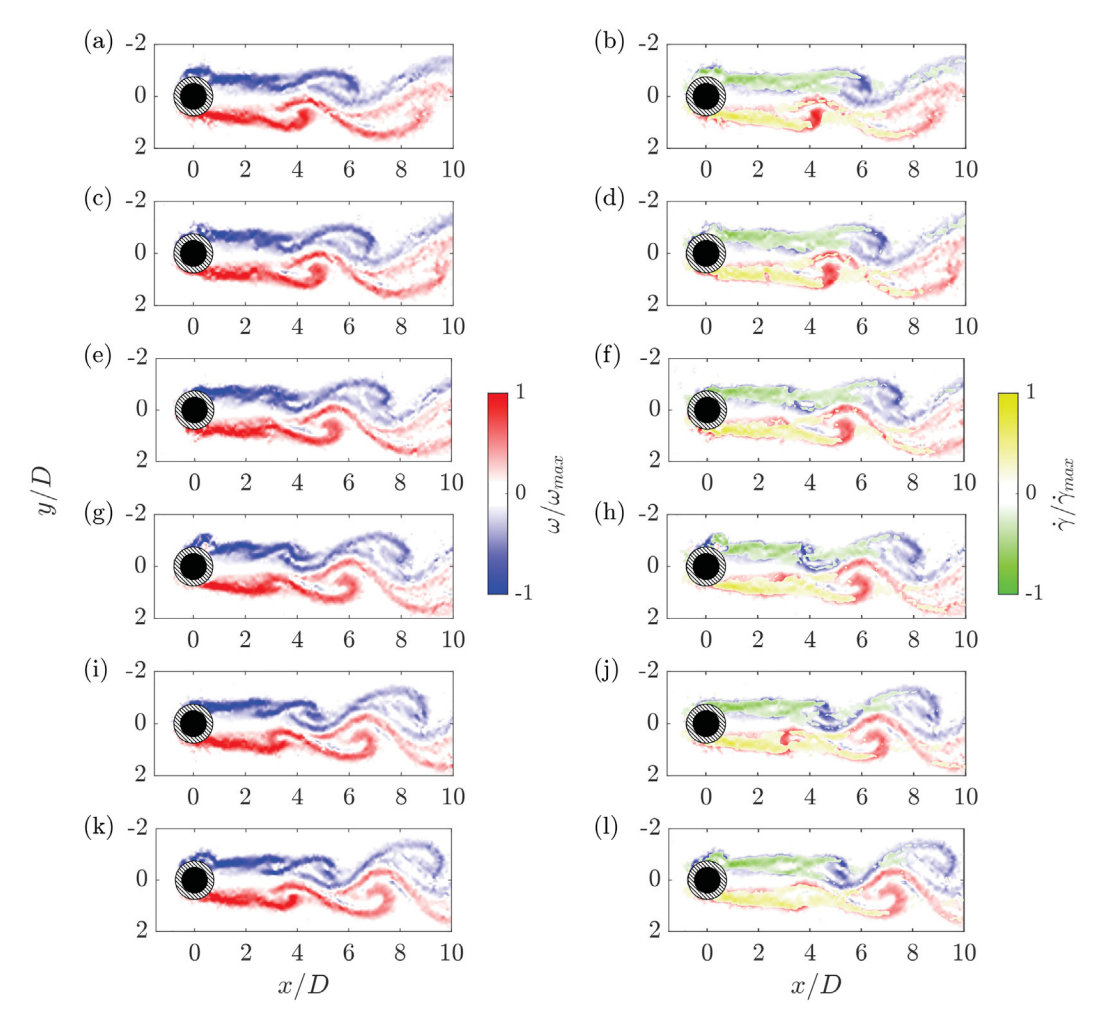


Fig. 3. The wake of a fixed cylinder at Re = 726, Wi = 2.2, and El = 3.0 for c = 0.02 g/L shown in the form of vorticity (left) and with shear rate overlayed on vorticity (right) at (a, b) 0%, (c, d) 20%, (e, f) 40%, (g, h) 60%, (i, j) 80%, and (k, l) 100% of the shedding cycle. In the plots, $\omega_{max} = 240 \text{ s}^{-1}$ and $\dot{\gamma}_{max} = 227 \text{ s}^{-1}$. The hatched area represents the locations very close to the cylinder where the PIV results are not reliable.

Fig. 3(a and b), this is due to the fact that the tail of the previously shed vortex (the red tail) acts as a barrier. Numerical simulations of Patel et al. [38] have shown that large elastic stresses exist within the elongated tail likely leading to the reduction in vortex interaction. Furthermore, the shear rate in the head is significantly smaller than the shear rate in the tail of the previously shed vortex. In Fig. 3(c and d as well as e and f), the red vortex head moves further downstream and begins to curl over itself, but remains attached to the cylinder through a long red tail. Separation begins in Fig. 3(g and h as well as i and j) around $x/D \sim 3$ where the tail of the red vortex starts to roll, and produces an S-shaped pattern for the vortex. The tail then interferes with the vortex that is being formed in the next cycle (Fig. 3(k,l)), and isolates it from the vortex with the opposite sign. This cycle repeats on both sides of the cylinder. The vortex has been stretched to almost 4D in length with the largest shear rates, and therefore the largest accumulation of elastic stress in the entire shedding cycle occurs in the attached shear layer.

Snapshots of the wake for c=0.02 g/L and c=0.03 g/L at various combinations of Reynolds and Weissenberg numbers are shown in Fig. 5. For both fluid concentrations, the cylinder wake is stable at the first Reynolds numbers shown (Re=151 for c=0.02 g/L and Re=215 for c=0.03 g/L) and becomes unstable for the second Reynolds number shown (Re=238 for c=0.02 g/L and Re=317 for c=0.03 g/L). The corresponding Weissenberg numbers are presented in the Figure caption. The critical Reynolds number for the onset of shedding is much larger in cases shown here in comparison with both

a Newtonian fluid and a shear thinning fluid with similar power law exponent [17]. In fact for a Newtonian fluid, the critical Reynolds number for vortex shedding, $Re_{crit}=47$, is significantly smaller than the value observed here. Thus, it is clear that fluid elasticity stabilizes the wake of a fixed cylinder in cross flow.

As the Reynolds and Weissenberg numbers continue to increase, the maximum vorticity as well as the vortex formation length increase. The vortex formation length, L, is determined through measuring the recirculation bubble length, which is the boundary in the wake where the time average components of flow are equal to u=v=0. These values are given in Fig. 6. From these results, it is apparent that increasing the fluid elasticity at a fixed Reynolds number by increasing the polymer concentration increases the vortex formation length slightly. Additionally, unlike Newtonian fluids where increasing Reynolds number causes a decrease in formation length, increasing Reynolds number for a viscoelastic fluid increases vortex formation length because increasing Reynolds number is accompanied by a corresponding increase in Weissenberg number and elastic stress in the fluid.

To better illustrate the changes in vortex interactions and to calculate the shedding frequency and Strouhal number, we plot the vorticity in the wake of the cylinder at a distance of x/D=4 downstream of the cylinder and over a range of locations from y/D=-2 to y/D=2 as a function of time in Fig. 7. The outer peaks correspond to the vortex head and the inner peaks correspond to the vortex tails. The S-shapes that are observed in these time histories represent the entire vortex. For

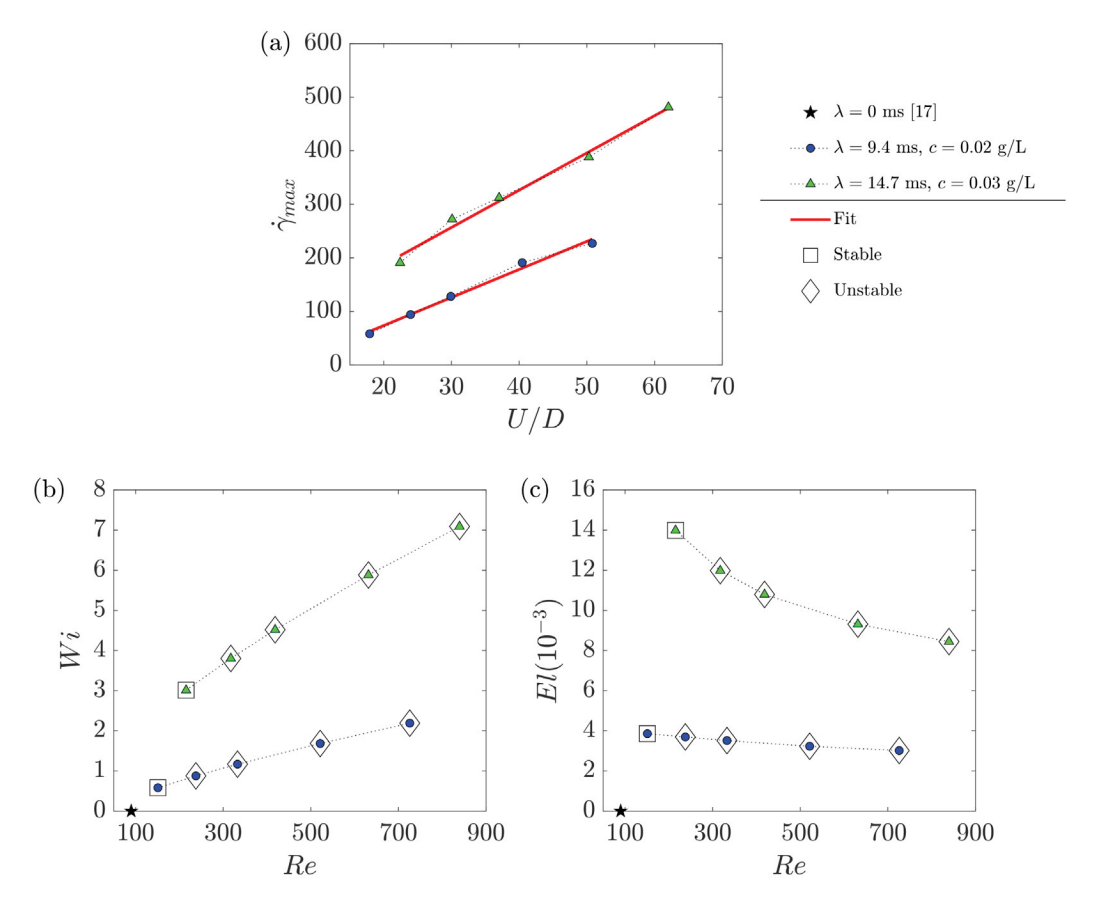


Fig. 4. (a) Maximum shear rate, \dot{r}_{max} , as a function of U/D, (b) the Weissenberg number, Wi, and (c) the elasticity number, El, as a function of Re for a fixed cylinder placed in c = 0.02 g/L and c = 0.03 g/L Flopaam solution. The stars correspond to the values for an inelastic fluid with similar shear behavior [17].

both c = 0.02 g/L and c = 0.03 g/L, in Fig. 7a, no shedding is observed at Re = 151 and Wi = 0.6 and Re = 215 and Wi = 3.0, respectively. Then as Reynolds and Weissenberg numbers are increased to Re = 238 and Wi = 0.9 for c = 0.02 g/L and Re = 317 and Wi = 3.8 for c = 0.03 g/L, shedding is observed. The periodic pattern that shows up in these plots corresponds to the shedding of vortices. The frequency of shedding is calculated from these time histories and presented as a non-dimensional Strouhal number in Fig. 8. For both cases, the shedding frequency increases as Re and Wi are increased further, however, as shown in Fig. 8, the Strouhal number remains roughly constant, independent of the Reynolds number. Fig. 8 confirms that viscoelasticity reduces the shedding frequency, as had been observed before for other viscoelastic fluids. The Strouhal number for the Newtonian fluid is $St \approx 0.2$ over the range of Reynolds numbers considered here. The Strouhal number drops to $St \approx 0.18$ for c = 0.02 g/L and $St \approx 0.17$ for c = 0.03 g/L, and stays relatively constant over this range of Reynolds numbers, which means that for these viscoelastic fluids too, the shedding frequency from a fixed cylinder increases linearly with increasing flow velocity.

5. Newtonian VIV as a basis for comparison

In this section, we present the Newtonian VIV response of the system for a series of constant Reynolds number cases. The reason to present these results here is that no previous set of experimental work at a constant Reynolds number and within this range of Reynolds numbers exists in the literature. The overall VIV behavior that is observed is similar to the general VIV behavior of any 1 DOF cylinder placed in flow, however the specific values for the range of the lock-in range as well as the amplitude of oscillations are not necessary the same.

The amplitude and frequency responses of VIV in Newtonian fluid (water) are presented in Fig. 9 for $100 \le Re \le 400$. The amplitude is

normalized by the cylinder diameter, so that $A^* = A/D$, where A is the oscillation amplitude, and the frequency response is normalized by the natural frequency in air, so that $f^* = f_{osc}/f_n$, where f_{osc} is the oscillation frequency. The amplitude and frequency responses follow what is typically observed in the VIV response of a flexibly-mounted cylinder in water [3,4]. The lock-in range begins at a $U^* \approx 6.1$ for Re = 100 and $U^* \approx 5.5$ for Re = 400. The oscillation amplitudes then increases rapidly and the maximum amplitude of $A^* \approx 0.5$ is reached in the range of $6.5 < U^* < 6.9$ for all Reynolds numbers. As U^* is increased, the amplitude decreases at a steeper slope for lower Reynolds numbers. The previous experimental results in the supercritical Reynolds number range (i.e., Re > 47) have been conducted such that the Reynolds number changes along the lock-in range, since the reduced velocity is increased by increasing the incoming flow velocity, and are typically conducted at larger Reynolds number ranges. By increasing the Reynolds number, the sharp decrease in the amplitude transitions to a slower initial decrease of the amplitudes, resembling a plateau at $A^* \approx 0.4$, followed by a sudden drop of amplitude at the end of the lock-in range—a trend that is more often observed in the experimental results of VIV responses at higher Reynolds numbers. Lock-in ends for all Reynolds numbers at U^* values between 9.4 and 9.9. Note that for Reynolds numbers of Re = 300 and higher, the results become essentially independent of Reynolds number for Newtonian fluids.

The reduced frequency response, f^* , is similar at all Reynolds numbers tested. It stays close to $f^* \approx 1$ over the entire lock-in range. The frequency starts at a value slightly below one and increases slowly to a value slightly larger than one as U^* is increased. This is typically observed in VIV responses of Newtonian fluids. The plateau of the reduced frequency reaches slightly higher values at higher Reynolds numbers, but the maximum difference in the f^* plateau at Re=100 and Re=400 is only roughly $\Delta f^* \approx 0.03$.

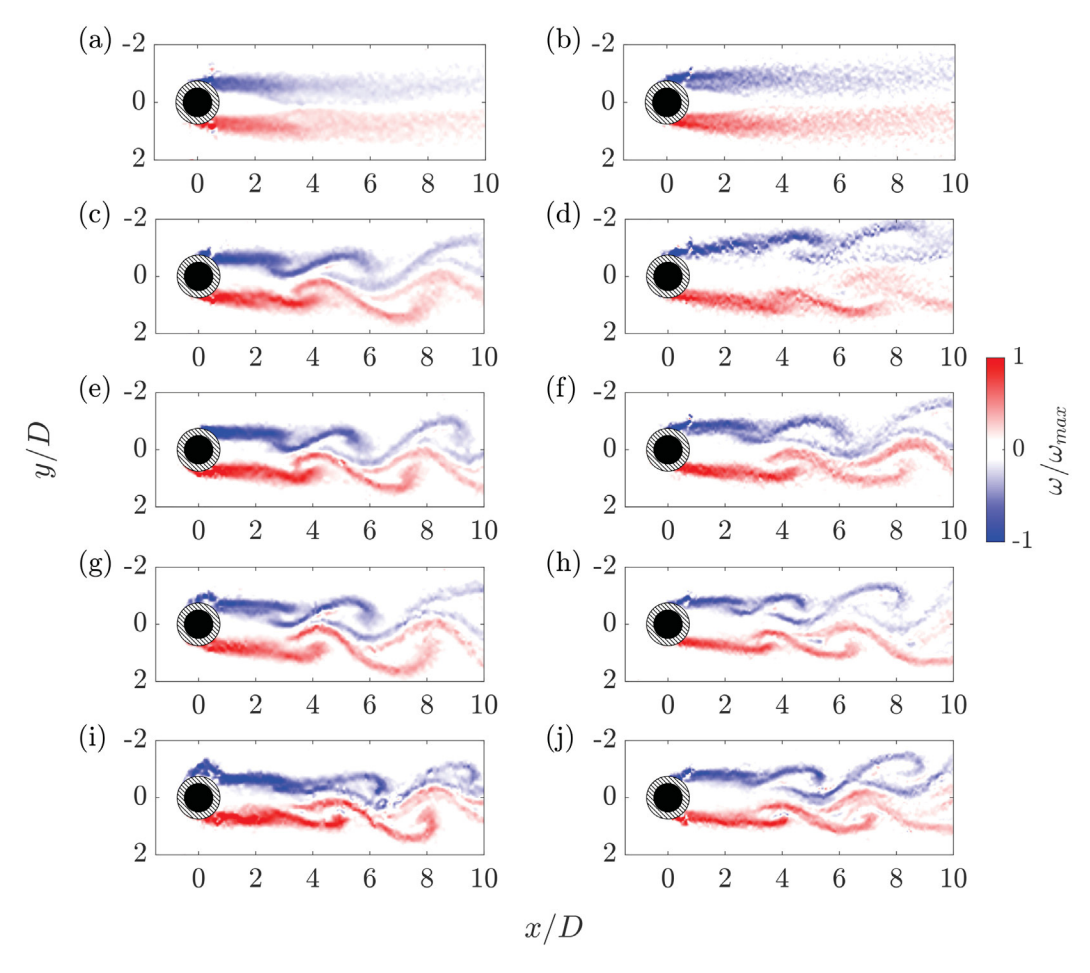


Fig. 5. The wake of a fixed cylinder at c = 0.02 g/L (left column) and c = 0.03 g/L (right column) and different Reynolds and Weissenberg numbers: (a) Re = 151, Wi = 0.6. (b) Re = 215, Wi = 3.0. (c) Re = 238, Wi = 0.9. (d) Re = 317, Wi = 3.8. (e) Re = 333, Wi = 1.2. (f) Re = 419, Wi = 4.5. (g) Re = 521, Wi = 1.7. (h) Re = 632, Re = 521, R

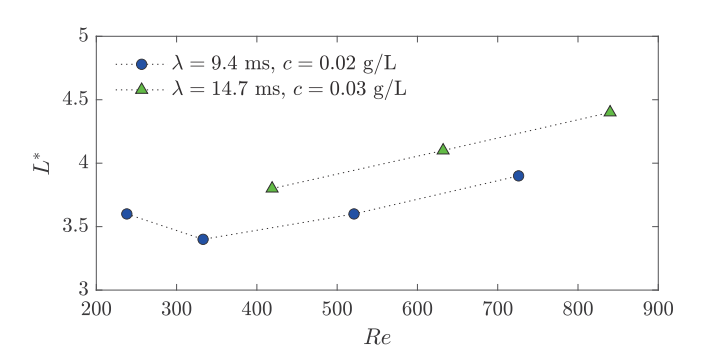


Fig. 6. Normalized formation length, $L^* = L/D$, of a fixed cylinder for c = 0.02 and c = 0.03 g/L measured from the center of the cylinder.

Sample snapshots of the wake of the cylinder undergoing VIV are shown in Fig. 10 for the two extreme Reynolds numbers that we have considered here: Re=100 and Re=400. At $U^*=5$ (the first row of the figure), the lock-in has not started yet, and the cylinder does not yet oscillate, and as a result, the shedding that is observed is at a frequency predicted by the Strouhal law for the shedding off a fixed cylinder. Note the large difference in the formation lengths between the two Reynolds number and that the trend with Reynolds number is opposite of what was observed for the fixed cylinder in the viscoelastic fluids in

the previous section. At $U^*=6.5$ (the second row of the figure), the oscillation amplitude is at its maximum, two single vortices are shed in the wake of the cylinder. These vortices are shed at a frequency equal to the oscillation frequency. At the highest reduced velocity shown here, $U^*=9$ (the third row of the figure), still two vortices are shed in each cycle, however, the distances between vortices become larger in comparison with the previous reduced velocity.

6. The amplitude and frequency of viscoelastic VIV

The amplitude and frequency responses for c = 0.02 and c = 0.03g/L cases are shown in Fig. 11 over a range of 151 \leq Re \leq 840 and $0.6 \le Wi \le 7.1$. The differences between the viscoelastic VIV and Newtonian VIV in Fig. 9 are clearly observed in terms of the amplitudes of oscillations, the width, onset and end of the lock-in range, as well as the overall shape of the amplitude response versus the reduced velocity. The maximum oscillation amplitude at the highest Reynolds numbers studied reduces from $A^* = 0.5$ for the Newtonian case to $A^* = 0.16$ for the c = 0.02 g/L Flopaam solution. The maximum observed amplitude of oscillations decreases even further with increasing fluid elasticity from $A^* = 0.16$ for the c = 0.02 g/L Flopaam solution to $A^* = 0.06$ for the c = 0.03 g/L Flopaam solution. The oscillations for the c = 0.03g/L Flopaam solution are at the lower limit of what could be measured experimentally. For $Re \le 151$ in the case of c = 0.02 g/L Flopaam solutions, and $Re \le 215$ in the case of c = 0.03 g/L Flopaam solutions, no oscillations of the cylinder are observed. At those same Reynolds numbers, large amplitude oscillations are observed in the Newtonian

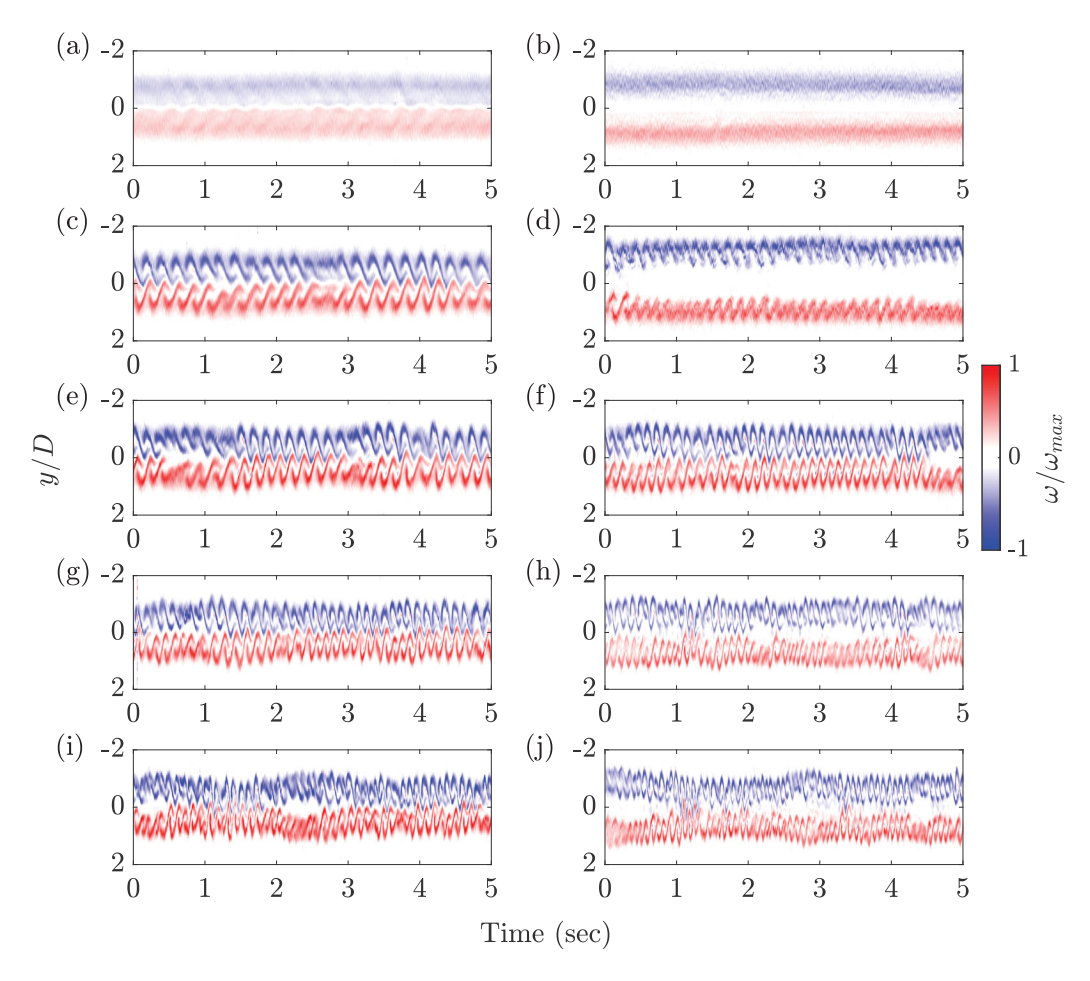


Fig. 7. Vorticity over the y/D direction as a function of time at x/D = 4 for c = 0.02 g/L (left column) and c = 0.03 g/L (right column) at different Reynolds and Weissenberg numbers: (a) Re = 151, Wi = 0.6. (b) Re = 215, Wi = 3.0. (c) Re = 238, Wi = 0.9. (d) Re = 317, Wi = 3.8. (e) Re = 333, Wi = 1.2. (f) Re = 419, Wi = 4.5. (g) Re = 521, Wi = 1.7. (h) Re = 632, Wi = 5.9. (i) Re = 726, Wi = 2.2. (j) Re = 840, Wi = 7.1. The maximum vorticities in these plots are (a, b) $\omega_{max} = 75$ s⁻¹, (c, d) $\omega_{max} = 112$ s⁻¹, (e, f) $\omega_{max} = 130$ s⁻¹, (g, h) $\omega_{max} = 217$ s⁻¹, and (i, j) $\omega_{max} = 240$ s⁻¹.

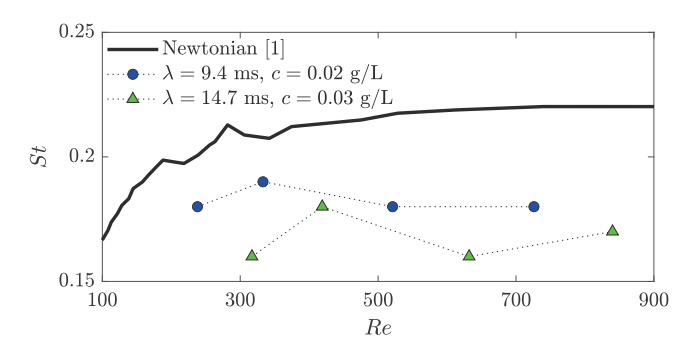


Fig. 8. Strouhal number as a function of Reynolds number for Newtonian flow [1], and viscoelastic flows used here, c=0.02 g/L, and c=0.03 g/L.

case. Thus, viscoelasticity can fully suppress VIV at low to moderate Reynolds numbers. Additionally, increasing fluid viscoelasticity by increasing polymer concentration increases the critical Reynolds number necessary to observe VIV. With the right polymer additives, it would be possible to increase VIV suppression to even larger Reynolds numbers. This was, in fact, observed for a c=0.05 g/L Flopaam solution, not presented here, that showed complete VIV suppression over the entire range of Reynolds numbers tested, $Re \leq 700$.

As observed in Fig. 11, the form of the oscillation amplitude curve for the viscoelastic fluids within the lock-in range is very different from the typical Newtonian response shown in Fig. 9. For the viscoelastic

cases, a plateau in the oscillation amplitude is not observed within the lock-in range. Instead, the oscillation amplitude increases monotonically with increasing reduced velocity until it reaches a maximum. For the lower Reynolds numbers tested for the c = 0.02 g/L Flopaam solution, the oscillation amplitude increases rapidly then decreases slowly to zero over one or two units of reduced velocity. For the larger Reynolds numbers tested, Re > 521, the decrease in oscillation amplitude is quite sharp and sudden. The sudden drop in the magnitude observed at $U^* = 5$ in the case of the c = 0.02 g/L Flopaam solution at Reynolds numbers larger than Re > 521 is likely directly related to the elasticity on the fluid. With increasing Reynolds number, the Weissenberg number also increases leading to increased elastic stress. In these cases, for Re > 521, the Weissenberg number is greater than Wi > 1.7. However, elastic stress does not just depend on Weissenberg number. Elastic stresses build up with time or strain. If the oscillation frequency is too high, elastic stresses do not have sufficient time to build up, reach steady state and impart their maximum effect on the flow. The Deborah number, $De = \lambda f_{osc}$, can be used to determine whether elastic stresses have had sufficient time to reach steady state. At a large Deborah number, the elastic stresses of the fluid are far from equilibrium. While at a small Deborah number, De < 1, the fluid elastic stresses have sufficient time to become fully developed. This analysis was used by Patel et al. [38] to demonstrate numerically that for a viscoelastic liquid, the elastic stresses can be built up as the oscillation frequency is reduced, and the reduced velocity, U^* , is increased.

Within the lock-in range, where $f_{osc} = f_n$, De is inversely proportional to U^* such that $De = \lambda U/DU^*$. For the c = 0.02 g/L Flopaam

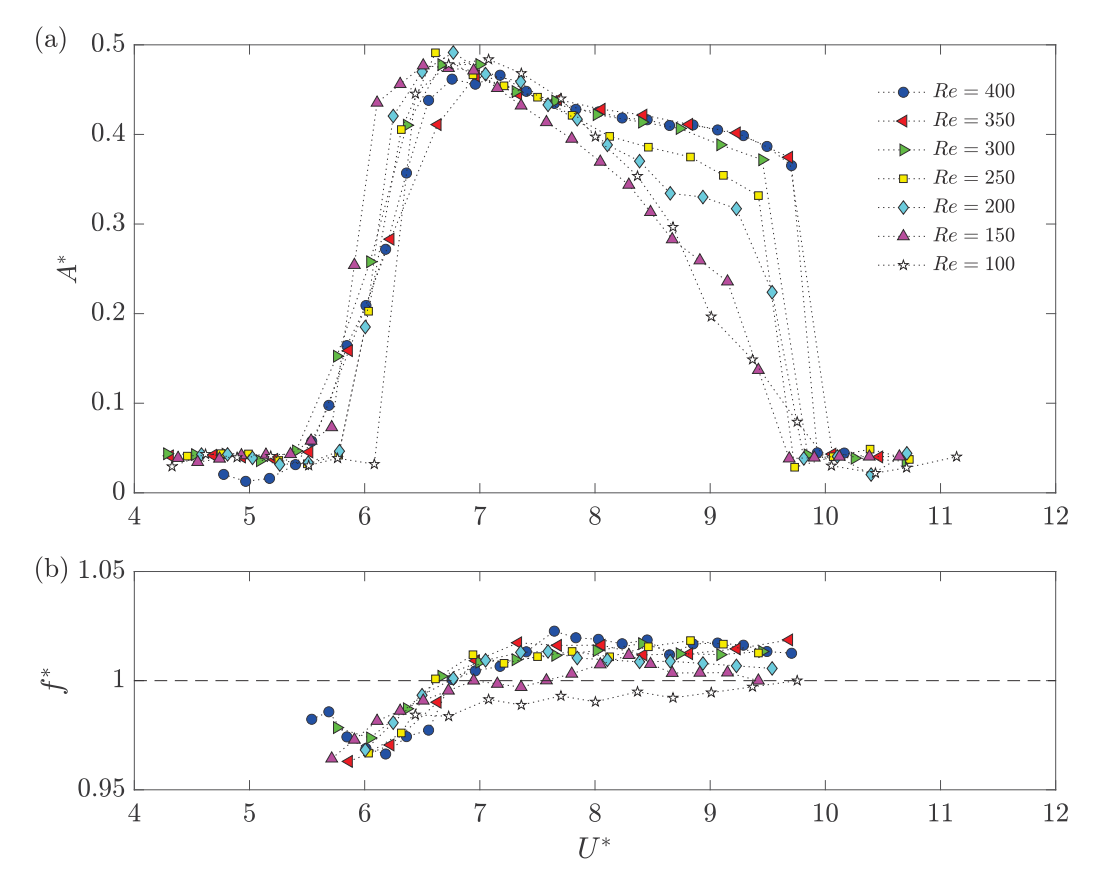


Fig. 9. (a) Amplitude and (b) frequency responses of a flexibly-mounted cylinder placed in Newtonian flow of water in the Reynolds number range of $100 \le Re \le 400$.

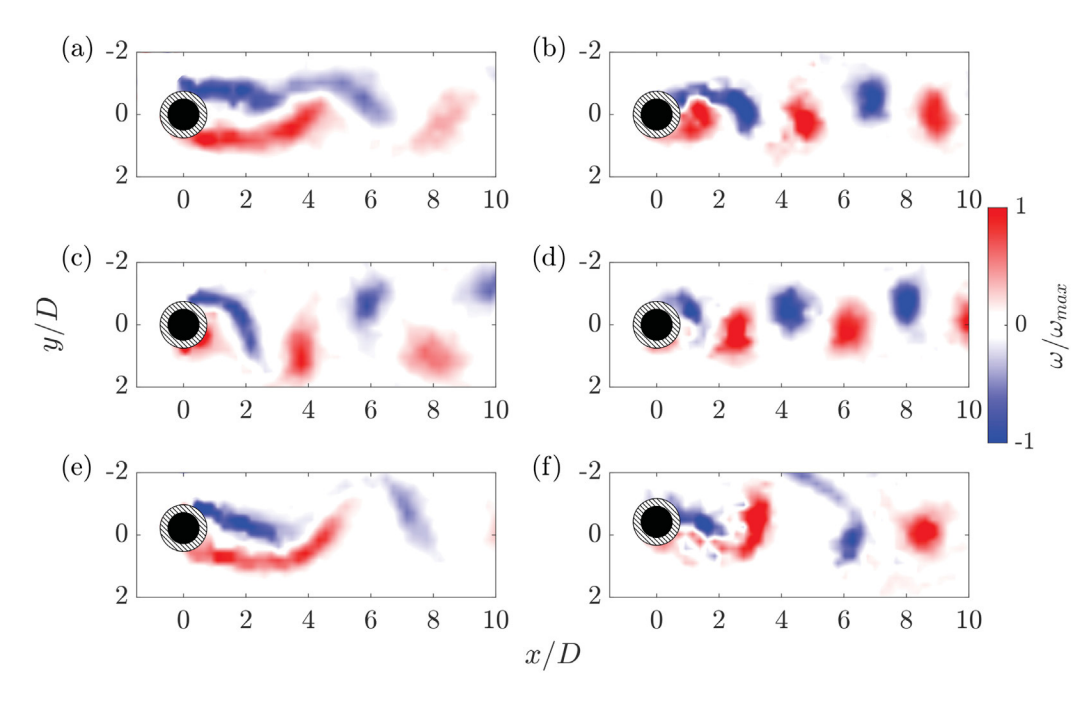


Fig. 10. Sample snapshots of the wake of a flexibly-mounted cylinder undergoing VIV in Newtonian flow at Re = 100 (left column) and Re = 400 (right column) and at three reduced velocities: $U^* = 5$ (first row), $U^* = 6.5$ (second row), and $U^* = 9$ (third row).

solution, the Deborah number can also be related to the Weissenberg number such that $De=Wi/4U^*$ for c=0.02 g/L and $De=Wi/8U^*$ for c=0.03 g/L. Thus for the case of Re=726 and Wi=2.2, the observed sharp transition in oscillation amplitude occurs when

the Deborah number is roughly $De \approx 0.1$. As seen in the data, with decreasing Weissenberg number, this transition occurs at smaller and smaller U^* which translates into roughly the same Deborah number for each case, $De \approx 0.1$. This observation lends credence to our hypothesis

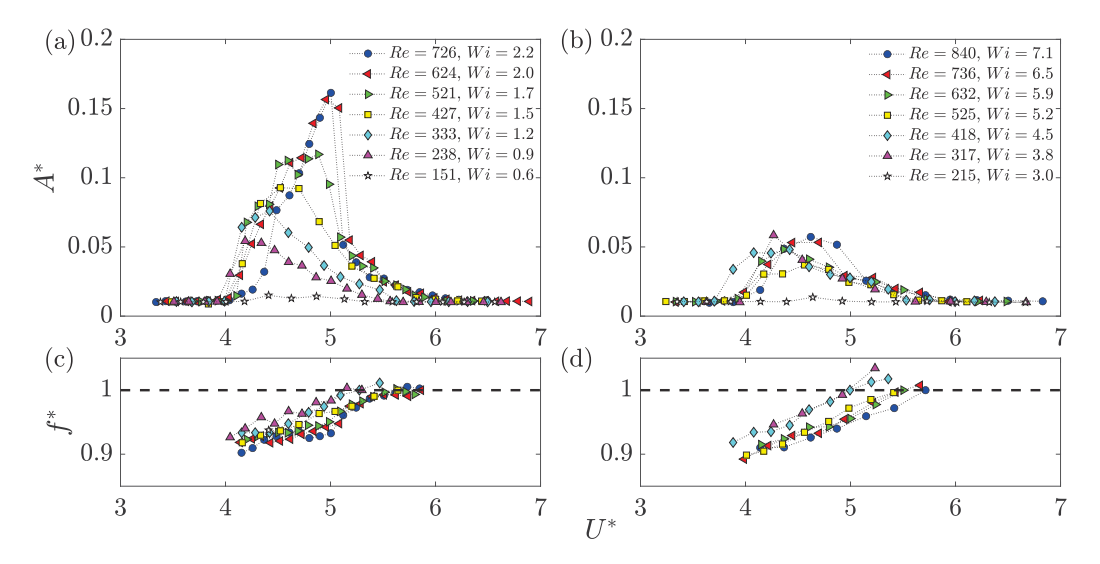


Fig. 11. Amplitude and frequency responses of a flexibly-mounted cylinder placed in viscoelastic flow: c = 0.02 g/L (left column) and c = 0.03 g/L. (right column).

that for elasticity to maximally affect VIV, the elastic stresses require sufficient time during the oscillation cycle to approach steady state.

In general, the drop in the magnitude within the lock-in range in comparison with the Newtonian case is significant for both viscoelastic cases shown here. The maximum amplitude observed for the case of c=0.02 g/L Flopaam solution is around $A^*=0.18$ and the maximum amplitude observed in the case of c=0.03 g/L Flopaam solution is only around $A^*=0.07$. Oscillations of amplitude less than $A^*<0.1$ are often considered negligible in the crossflow VIV responses of Newtonian fluids.

The width of the lock-in range for both viscoelastic fluids was found to be significantly smaller than that of a typical Newtonian fluid. For a Newtonian fluid, lock-in occurs in the reduced velocity range of $5.7 \le U^* \le 9.8$, while for the viscoelastic fluids studied here, this range is reduced to $4.0 \le U^* \le 5.7$. Also, the onset of lock-in for the viscoelastic fluids shifts to lower reduced velocities, from $U^* = 5.7$ to $U^* = 4.0$, but stays at the same reduced velocity independent from the Reynolds and Weissenberg number. This is expected due to the fact that the Strouhal numbers reported for these fluids in Section 4 stay constant in this range of Reynolds and Weissenberg numbers. It is the value of the Strouhal number that controls the onset of lock-in in a VIV response. We had shown previously [17] that for a purely shearthinning fluid, the lock-in range shifts to smaller reduced velocities with increasing Reynolds number. This was due to the fact that the shedding frequency of a purely shear-thinning fluid increases with increasing Reynolds number, and as a result the synchronization between the shedding frequency and the system's natural frequency occurs at lower reduced velocities, U^* . In a purely elastic fluid, however, the shedding frequency has been found to decrease with increasing Reynolds number [10,12-14,16]. Since in the fluids considered here both elastic and shear-thinning effects are at the play, it appears that the competition between the two has roughly canceled each other out and resulted in the start of the lock-in range being at the same reduced velocity independent of Reynolds and Weissenberg numbers.

The normalized frequency, f^* , is presented in Fig. 11 (lower row) for both the viscoelastic solutions tested here. At the beginning of the lock-in range the normalized frequency is $f^*\approx 0.9$ and it increases with increasing U^* until it reaches $f^*=1$ toward the end of the lock-in range. As opposed to the response of the Newtonian case, the normalized frequency never reaches a plateau at $f^*=1$, but it is still close to one and the PIV measurements show clear synchronization between the shedding frequency and oscillation frequency confirming that lock-in has been achieved. The deviation from one is likely due to the fact that f^* is normalized with respect to the natural frequency

of the cylinder in air and not in the viscoelastic fluids we are studying here. The natural frequency of the system in these viscoelastic fluid is expected to be smaller than that in air, which implies had f^* been normalized with respect to the natural frequency in fluid, it would have resulted in larger values at the beginning of the lock-in range and would have been closer to one.

7. The wake in the viscoelastic cases

The wake of the cylinder in viscoelastic flow at $U^*=4.75$ is shown in Fig. 12 over one cylinder oscillation cycle for both the c=0.02 g/L Flopaam solution (at Re=238 and Wi=0.9) and the c=0.03 g/L Flopaam solution (at Re=317 and Wi=3.8). These cases exhibit oscillations of very small amplitudes, less than $A^*=0.05$ for both viscoelastic fluids, which explains why the wake in both cases resembles the wake of a fixed cylinder placed in viscoelastic fluids (Fig. 5), where the vortices are elongated and have a tail, which influences the formation of the next vortex of the same sign, clearly, very different from those observed in the wake of the cylinder in Newtonian fluid shown in Fig. 10. For the case with higher elasticity (c=0.03 g/L), the wake is wider, similar to what had been observed previously in the wake of the fixed cylinder. The formation of these vortices exerts a periodic force on the cylinder and causes oscillations—although with very small amplitudes.

At a higher Reynolds numbers and at the same Reduced velocity, $U^* = 4.75$, the wake is very different. In Fig. 13, the wakes for one cylinder oscillation cycle for both the c = 0.02 g/L Flopaam solution (at Re = 726 and Wi = 2.2) and the c = 0.03 g/L Flopaam solution (at Re = 840 and Wi = 7.1) are shown. At these Reynolds numbers, narrow wakes are formed behind the cylinder in each fluid. Note that the amplitude of oscillations is larger than the previous cases shown, but still much smaller than for a Newtonian fluid. When the fluid is less elastic, the vortices are formed closer to each other in the wake. Patel et al. [38] showed that an elastic stress forms along the exterior of the vortices, which influences the roll-up dynamics of the vortex. If a fluid is more elastic, the vortices are not able to roll up as tightly, which decreases the strength of the vortex. This also influences the width of the wake: the less elastic fluid has a wider wake. The stronger vortices that are formed in the case of the c = 0.02 g/L Flopaam solution likely lead to the larger amplitude of oscillations observed in this case.

8. Conclusions

We study the VIV response of a flexibly-mounted rigid cylinder in inertia-viscoelastic flows. Previous studies on VIV of such systems have

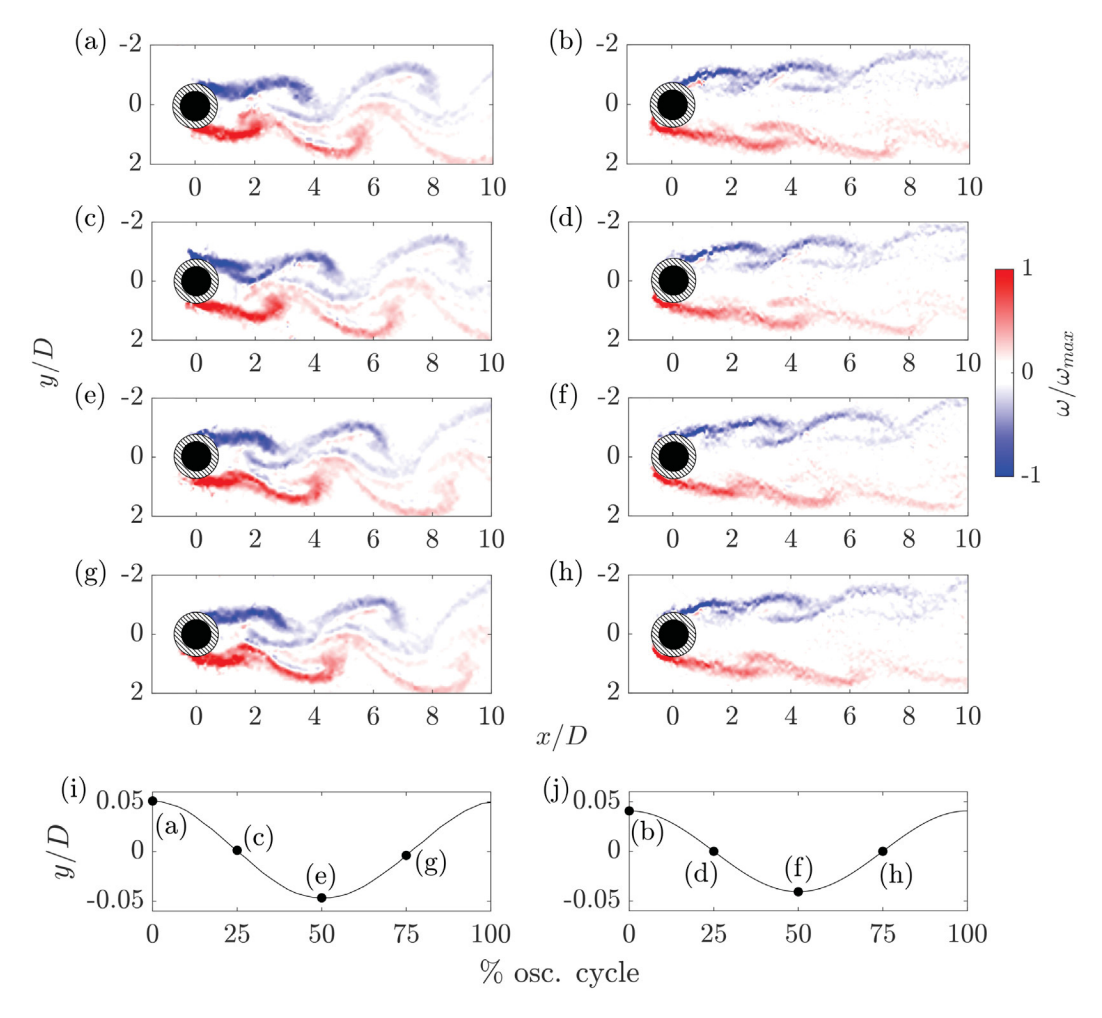


Fig. 12. Snapshots of the wake of the flexibly-mounted cylinder at $U^* = 4.75$ for the c = 0.02 g/L Flopaam solution at Re = 238 and Wi = 0.9 (left column) and the c = 0.03 g/L Flopaam solution at Re = 317 and Wi = 3.8 (right column) at four instances within one cycle of oscillations: (a, b) 0%, (c, d) 25%, (e, f) 50%, and (g,h) 75% of the cycle. (i,j) A cycle of oscillations. In the plots, the vorticity is normalized by $\omega_{max} = 117$ s⁻¹.

been conducted for cases where either fluid inertia or fluid elasticity are dominant, i.e., $Re\gg 1$ and Wi<1 or $Re\ll 1$ and Wi>1. In this work, both fluid inertia and elasticity are significant. We have conducted a series of VIV experiments using viscoelastic fluids that are made by mixing the Flopaam in distilled water at two different concentrations: c=0.02 g/L and c=0.03 g/L. For the fluid that we use here, increasing the Reynolds number is accompanied by an increase in the Weissenberg number. To define the Reynolds number, we use the maximum shear rate observed in the wake from our PIV measurements, and therefore the exact Reynolds number is not known a priori, and is calculated after the experimental data are analyzed.

At each Flopaam concentration, we show that the Reynolds number influences the VIV response. It is known for a Newtonian fluid that VIV is observed at Reynolds numbers larger than a critical, i.e., Re=19. This is also observed here, for both flow concentrations, however, the critical Reynolds numbers for the onset of VIV in the viscoelastic flows considered here are $Re\approx150$ and $Re\approx215$, respectively, for c=0.02 g/L and c=0.03 g/L concentrations. For Reynolds numbers larger than the critical, in the case of c=0.02 g/L, the VIV amplitude increases with increasing Reynolds number up to Re=625 after which the VIV response seems to be independent from the Reynolds number. This is also similar to the VIV response of a Newtonian case where for post-critical Reynolds numbers, the VIV response increases with increasing Reynolds number initially and then reaches a plateau. In the case of c=0.03 g/L, however, although the VIV response is indeed observed for Reynolds numbers larger than the critical, the amplitude of oscillations

remains very small (i.e., $A^*\approx 0.05$) and no major increase in the amplitude is observed versus the Reynolds number.

The onset of VIV response for the viscoelastic cases do not depend on the Reynolds number. This is also reflected in our measurements of the Strouhal number in the wake of fixed cylinders placed in these flows in the same range of Reynolds numbers. Those measurements show that the Strouhal number stays more or less constant within this range of Reynolds numbers, and since the onset of lock-in corresponds to when the shedding frequency and the system's natural frequency are equal, the onset of lock-in does not change with the Reynolds number, since the Strouhal number does not depend on the Reynolds number. This is different from previous observations on the VIV response of a purely shear thinning flow, and the VIV response of a purely viscoelastic flow. For shear thinning, VIV starts at smaller reduced velocities and for viscoelastic flows, it starts at higher reduced velocities. In the fluid that we use here, it seems that the competing effects of the two have canceled each other at least for the onset of the lock-in range.

The vortices that are observed in the wake of the cylinder in the case of viscoelastic flows are different from those observed in Newtonian flows. Elongated S-shaped vortices are observed in the wake in the case of these viscoelastic flows as opposed to the typical vortices that are observed in the von Karman Street in the wake of a cylinder placed in Newtonian flow. The tail of the viscoelastic vortices is elongated such that it intervenes with the formation of the vortices in the following cycle and prevents them from crossing the centerline of the wake and travel to the opposite side. The formation length in the case of a fixed

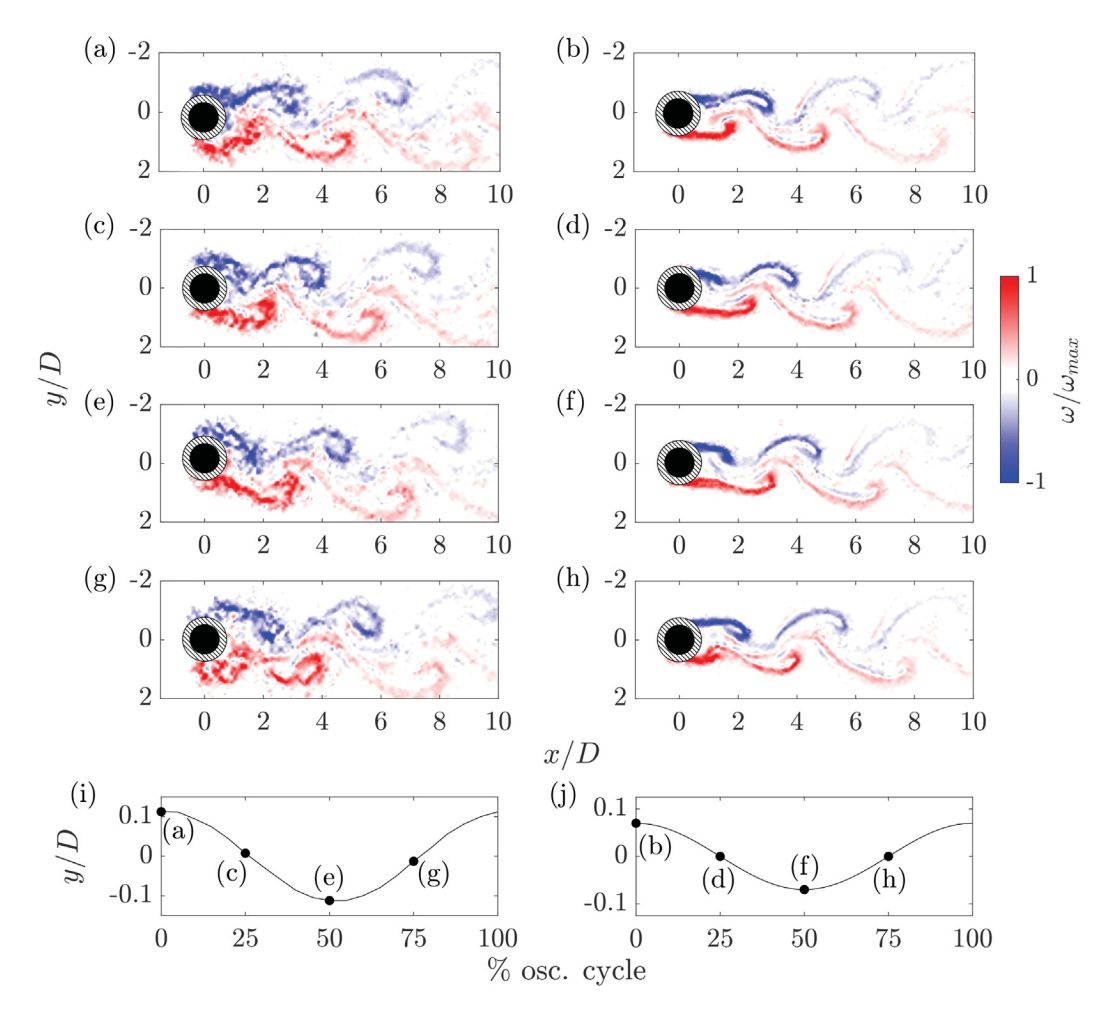


Fig. 13. Snapshots of the wake of the flexibly-mounted cylinder at $U^* = 4.75$ for the c = 0.02 g/L Flopaam solution at Re = 726 and Wi = 2.2 (left column) and the c = 0.03 g/L Flopaam solution at Re = 840 and Wi = 7.1 (right column). Four instances within one cycle of oscillation at (a, b) 0%, (c, d) 25%, (e, f) 50%, and (g,h) 75% of the cycle. (i,j) A cycle of oscillations. In the plots, the vorticity is normalized with $\omega_{max} = 280$ s⁻¹.

cylinder increases with the Reynolds number, but when oscillations are observed, the formation length decreases substantially and vortices form much closer to the cylinder.

A major outcome of this work is that adding elasticity to the fluid at a constant Reynolds number can suppress VIV completely. This is evident in the decrease of the amplitude of oscillations from $c=0.02\,$ g/L concentration to the $c=0.03\,$ g/L concentration. We also conducted a series of tests for a concentration of $c=0.05\,$ g/L, and observed no displacement for all Reynolds numbers that we considered.

CRediT authorship contribution statement

Pieter R. Boersma: Conceptualization, Data curation, Formal analysis, Methodology, Visualization, Writing – original draft. Jonathan P. Rothstein: Conceptualization, Formal analysis, Funding acquisition, Supervision, Writing – review & editing. Yahya Modarres-Sadeghi: Conceptualization, Formal analysis, Funding acquisition, Supervision, Writing – review & editing.

Declaration of competing interest

The authors declare that they have no known competing financial interests or personal relationships that could have appeared to influence the work reported in this paper.

Data availability

Data will be made available on request.

Acknowledgments

This work was funded by the National Science Foundation, USA under Grant No. CBET-2126175.

Appendix

Figs. A.1, A.2, A.3, and their corresponding Tables A.1, A.2, A.3, show how U^* , f_n , ζ , and m^* vary over the range of Reynolds numbers tested here and for varying lengths of the springs for the Newtonian case as well as the viscoelastic cases with c=0.02 g/L and c=0.03 g/L. As U^* increases, the length of the spring increases, which decreases f_n and ζ , and increases m^* .

Table A.1 Newtonian case — Summary of f_n , ζ , and m^* for $100 \le Re \le 400$ and $4.3 \le U^* \le 11.1$.

reviolitai case	building of j_n , ς , ι i	id m 101 100 3 1tc 3 400 th	101 100 3 1tc 3 400 tilta 4.5 3 0 3 11.11.		
Re (-)	f_n (Hz)	ζ (–)	m* (-)		
100	2.3-6.2	0.011-0.013	26.9-33.3		
150	3.6-9.0	0.011-0.015	25.5-29.8		
200	4.9-11.9	0.012-0.020	24.6-28.1		
250	5.8-14.9	0.013-0.025	24.0-27.2		
300	7.1-18.6	0.014-0.028	23.4-26.3		
350	8.3-21.8	0.015-0.029	23.1-25.8		
400	9.9-21.8	0.016-0.029	23.1-25.2		

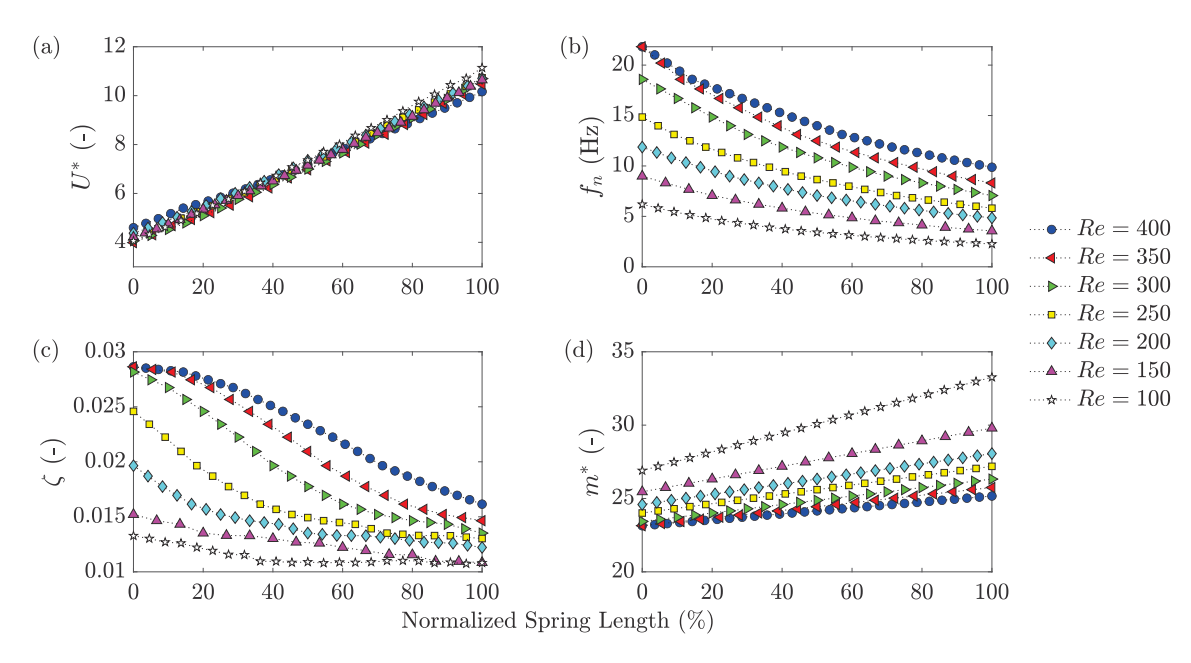


Fig. A.1. Newtonian case—Values of U^* , f_n , ζ , m^* as a function of normalized spring length where 0% is the spring length at the first U^* and 100% is the spring length at the last U^* .

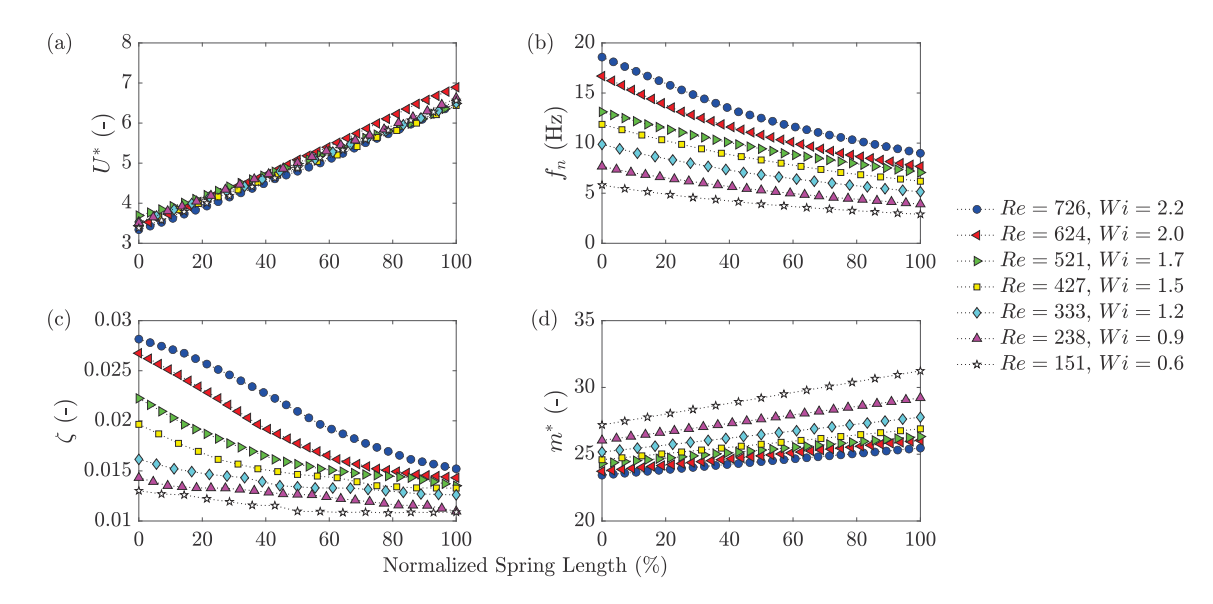


Fig. A.2. Viscoelastic case with c=0.02 g/L—Values of U^* , f_n , ζ , m^* as a function of normalized spring length where 0% is the spring length at the first U^* and 100% is the spring length at the last U^* .

Table A.2 Viscoelastic case with c=0.02 g/L — Summary of f_n , ζ , and m^* for $151 \le Re \le 726$ and $3.3 \le U^* \le 6.9$.

Re (-)	f_n (Hz)	ζ (–)	m^* (-)
151	2.9-5.8	0.011-0.013	7.7–8.7
238	3.9-7.7	0.011-0.014	7.4-8.2
333	5.1-9.9	0.013-0.016	7.2-7.8
427	6.2-11.9	0.013-0.020	7.0-7.6
521	7.1-13.1	0.03-0.022	7.0 - 7.5
624	7.7-16.7	0.014-0.027	6.8 - 7.4
726	9.0-18.6	0.015-0.028	6.7-7.2

Table A.3 Viscoelastic case with c=0.03 g/L — Summary of f_n , ζ , and m^* for $215 \le Re \le 840$ and $3.3 \le U^* \le 6.1$.

Re (-)	f_n (Hz)	ζ (–)	m* (-)	
215	3.7–7.7	0.011-0.014	7.4–8.3	
317	5.1-9.9	0.013-0.016	7.2-7.8	
418	6.6-13.1	0.013-0.022	7.0-7.5	
525	8.3-16.7	0.015-0.027	6.8-7.3	
632	9.0-18.6	0.015-0.028	6.7-7.3	
736	10.8-21.8	0.018-0.029	6.7-7.1	
840	10.8-21.8	0.018 - 0.029	6.7-7.1	

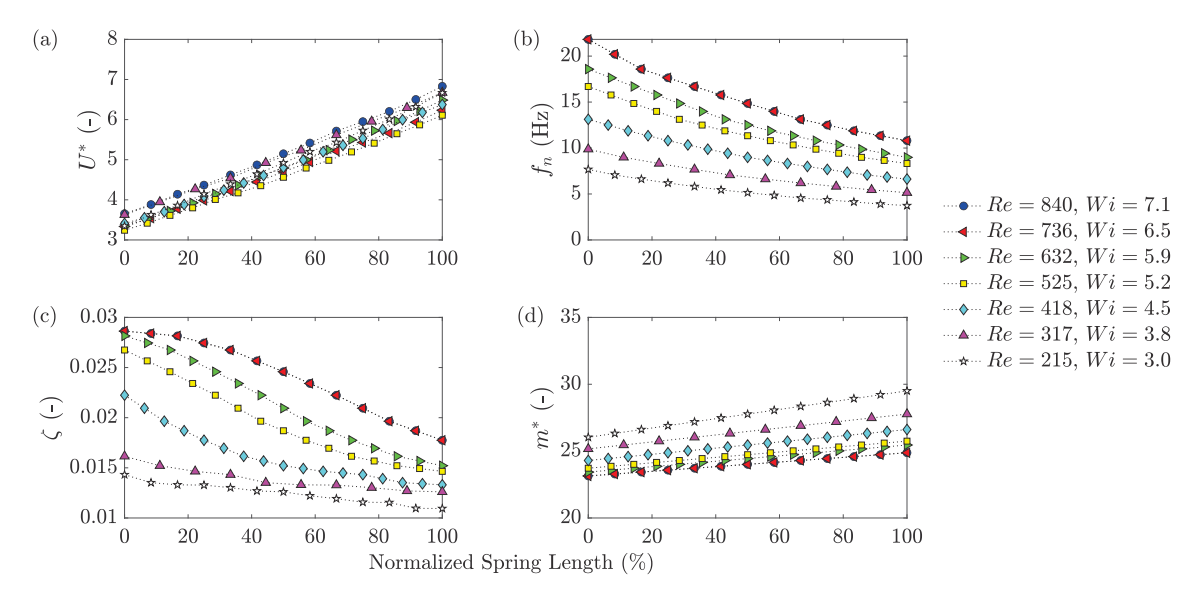


Fig. A.3. Viscoelastic case with c = 0.03 g/L—Values of U^* , f_n , ζ , m^* as a function of normalized spring length where 0% is the spring length at the first U^* and 100% is the spring length at the last U^* .

References

- [1] R.D. Blevins, Flow-induced vibrations, Krieger Publishing Company, 1990.
- [2] M.P. Païdoussis, S.J. Price, E.D. Langre, Fluid-Structure Interactions: Cross-Flow-Induced Instabilities, Cambridge University Press., 2014.
- [3] Y. Modarres-Sadeghi, Introduction To Fluid-Structure Interactions, Springer Nature. 2021.
- [4] C.H.K. Williamson, R. Govardhan, Vortex-induced vibrations, Annu. Rev. Fluid Mech. 36 (2004) 413–455.
- [5] T. Sarpkaya, A critical review of the intrinsic nature of vortex-induced vibrations, J. Fluids Struct. 19 (2004) 389–447.
- [6] C. Mathis, M. Provansal, L. Boyer, The bernard-von karman instability: an experiemntal study near the threshold, J. Physique Lett. 45 (1984) 483.
- [7] S. Mittal, S. Singh, Vortex-induced vibrations at subcritical Re, J. Fluid Mech. 534 (2005) 185.
- [8] P.R. Boersma, J.P. Rothstein, Y. Modarres-Sadgehi, Experimental evidence of vortex-induced vibrations at subcritical Reynolds numbers, J. Fluid Mech. 922 (2021) R3.
- [9] R. Bourguet, Vortex-induced vibrations of a flexible cylinder at subcrital Reynolds number, J. Fluid Mech. 902 (2005) R3.
- [10] P.M. Coelho, F.T. Pinho, Vortex shedding in cylinder flow of shear-thinning fluids. i. identification and demarcation of flow regimes, J. Non-Newton. Fluid Mech. 110 (2003) 143–176.
- [11] C. Pipe, P. Monkewtiz, Vortex shedding in flows of dilute polymer solutions, J. Non-Newton. Fluid Mech. 139 (2006) 54—67.
- [12] S. Bailoor, J.H. Seo, R. Mittal, Vortex shedding from a circular cylinder in shear-thinning carreau fluids, Phys. Fluids 31 (2019) 011703.
- [13] M. Alam, A. Raj, P.M. Khan, S. Kumar, S. Roy, Numerical simulation of flow of shear-thinning carreau fluid over a transversley oscillating cylinder, J. Fluid Mech. 921 (2021) A23.
- [14] Ç. Şahin, K. Atalık, Comparison of inelastic and elastic non-Newtonian effects on the flow around a circular cylinder in periodic vortex shedding, J. Non-Newton. Fluid Mech. 263 (2019) 1–14.
- [15] I. Lashgari, J.O. Pralits, F. Giannetti, First instability of the flow of shear-thinning and shear-thickening fluids past a circular cylinder, J. Fluid Mech. 701 (2012) 201–227
- [16] F. Hamid, C. Sasmal, R.P. Chhabra, Dynamic mode decomposition analysis and fluid-mechanical aspects of viscoelastic fluid flows past a cylinder in laminar vortex shedding regime, Phys. Fluids 34 (2022) 103114.
- [17] P.R. Boersma, J.P. Rothstein, Y. Modarres-Sadgehi, An experimental investigation of vortex-induced vibrations of a flexibly-mounted cylinder in shear- and extensional-thinning flows, Phys. Rev. Fluids 8 (2023) 044703.
- [18] U.N. Patel, J.P. Rothstein, Y. Modarres-Sadeghi, Vortex-induced vibration of a cylinder in inelastic shear-thinning and shear-thickening fluids, J. Fluid Mech. 934 (2022) A39.
- [19] A. Dey, Y. Modarres-Sadeghi, J. Rothstein, Experimental observation of viscoelastic fluid-structure interactions, J. Fluid Mech. 813 (2017) R5.
- [20] A. Dey, Y. Modarres-Sadeghi, J. Rothstein, Viscoelastic fluid-structure interactions between a flexible cylinder and wormlike micelle solution, Phys. Rev. Fluids 3 (2018) 063301.

- [21] A. Dey, A. Lindner, Y. Modarres-Sadeghi, J. Rothstein, Oscillations of a cantilevered micro beam driven by a viscoelastic flow instability, Soft Matter Published online (2020) 1227–1235.
- [22] A. Dey, Y. Modarres-Sadeghi, J. Rothstein, Viscoelastic flow-induced oscillations of a cantilevered beam in the crossflow of a wormlike micelle solution, J. Non-Newton. Fluid Mech. 286 (2020) 104433.
- [23] A. Dey, Y. Modarres-Sadeghi, J. Rothstein, Observation of lock-in for viscoelastic fluid-structure interactions, J. Fluids Struct. 96 (2020) 103025.
- [24] C. Hopkins, S. Haward, A. Shen, Purely elastic fluid-structure interactions in microfluidics: Implications for mucociliary flows, Small 16 (2020) 1903872.
- [25] S. Kenney, K. Poper, G. Chapagain, G. Christopher, Large deborah number flows around confined microfluidic cylinders, Rheol. Acta 52 (2013) 485–497.
- [26] J.P. Rothstein, G.H. McKinley, The axisymmetric contraction-expansion: The role of extensional rheology on vortex growth dyanmics and the enhanced pressure drop, J. Non-Newton. Fluid Mech. 98 (2001) 33–63.
- [27] G.H. McKinley, H. Peyman, A. Öztekin, Rheological and geometric scaling of purely elastic flow instabilities, J. Non-Newton. Fluid Mech. 67 (1996) 19–47.
- [28] C. Hopkins, A. Shen, S. Haward, Effect of blockage ratio on flow of a viscoelastic wormlike micellar solution past a cylinder in a microchannel, Soft Matter 18 (2022) 8856–8866.
- [29] G. Mompean, M. Deville, Unsteady finite volume simulations of oldroyd-b fluid through a three-dimensional planar contraction, J. Non-Newton. Fluid Mech. 72 (1997) 253–279.
- [30] S.C. Xue, N. Phan-Thien, R.I. Tanner, Three dimensional numerical simulations of viscoelastic flows through planar contractions, J. Non-Newton. Fluid Mech. 74 (1998) 195–245
- [31] L.E. Rodd, J.J. Cooper-White, D.V. Boger, G.H. McKinley, Role of the elasticity number in the entry flow of dilute polymer solutions in micro-fabricated contraction geometries, J. Non-Newton. Fluid Mech. 143 (2007) 170–191.
- [32] O. Cadot, M. Lebey, Shear insability inhibition in a cylinder wake by local injection of a viscoelastic fluid, J. Fluids Struct. 11 (1999) 494–496.
- [33] O. Cadot, S. Kumar, Experimental characterization of viscoelastic effects on twoand three-dimensional shear insabilities, J. Fluid Mech. 416 (2000) 151–172.
- [34] O. Cadot, Partial roll-up of a viscoelastic Kármán street, Eur. J. Mech. B/Fluids 20 (2001) 145–153.
- [35] Y.L. Xiong, C.H. Bruneau, H. Kellay, Drag enhancement and drag reduction in viscoelastic fluid flow around a cylinder, Europhys. Lett. 91 (2010) 64001.
- [36] Y.L. Xiong, C.H. Bruneau, H. Kellay, Flow past a cylinder in diluted polymer solutions, J. Phys.: Conf. Ser. 318 (2011) 092021.
- [37] D. Richter, G. Iaccarino, E.S.G. Shaqfeh, Effects of viscoelasticity in the high Reynolds number cylinder wake, J. Fluid Mech. 693 (2012) 297.
- [38] U.N. Patel, J.P. Rothstein, Y. Modarres-Sadeghi, Forced oscillations of a rigid cylinder in viscoelastic fluids, J. Fluid Mech. 975 (2023) A28.
- [39] Y.L. Xiong, S. Peng, M. Zhang, D. Yang, Numerical study on the vortex-induced vibration of a circular cylinder in viscoelastic fluids, J. Non-Newton. Fluid Mech. 272 (2019) 104170.
- [40] P. Shakeri, M. Jung, R. Seemann, Scaling purely elastic instability of strongly shear thinning polymer solutions. Phys. Rev. E 105 (2022) L052501.
- [41] F.A. Morrison, Understanding Rheology, Oxford University Press, 2001.
- [42] J. Dinic, L.N. Jimenez, V. Sharma, Pinch-off dynamics and drippingonto-substrate (DoS) rheometry of complex fluids, Lab Chip 17 (2017) 460

- [43] S. Sur, J.P. Rothstein, Drop breakup dynamics of dilute polymer solutions: Effect of molecula weight, concentration, and viscosity, J. Rheol. 62 (2018) 1245.
- [44] S.L. Anna, G.H. McKinley, Elasto-capillary thinning and breakup of model elastic liquids, J. Rheol. 45 (2001) 115–138.
- [45] W. Thielicke, R. Sonntag, Particle image velocimetry for MATLAB: Accuracy and enhanced algorithms in PIVlab, J. Open Res. Softw. 9 (2021).
- [46] P.J. Oliveira, Method for time-dependent simulations of viscoelastic flows: vortex shedding behind cylinder, J. Non-Newton. Fluid Mech. 101 (2001) 113–137.